University of Huddersfield Repository

Ren, Hongyu, Gao, Feng and Jiang, Xiangqian

Least-squares method for data reconstruction from gradient data in deflectometry

Original Citation

This version is available at http://eprints.hud.ac.uk/id/eprint/29138/

http://eprints.hud.ac.uk/

A new least-squares method for data reconstruction from gradient data in deflectometry

HONGYU REN,[1, 2] FENG GAO,[1,*] XIANGQIAN JIANG[1]

[1]*EPSRC Center, University of Huddersfield, Huddersfield, HD1 3DH, UK*
[2]*College of Mechatronic Engineering and Automation, National University of Defense Technology, Changsha, Hunan, 410073, China*
Corresponding author: x.jiang@hud.ac.uk

Least-squares integration (LSI) and radial basis function integration (RBFI) methods are widely used to reconstruct specular surface shape from gradient data in a deflectometry measurement. The traditional LSI method requires gradient data having a rectangular grid, and RBFI method is effective at handling small size measurement data set. Practically, the amount of gradient data is rather large and data grids are in quadrilateral shapes. With this in mind, a new LSI method is proposed to integrate gradient data, which is based on an approximation that normal vector of one point is perpendicular to the vector connecting points at either side. A small measurement data set integrated by RBFI method is employed as a supplementary constraint of the proposed method. Simulation and experimental results show that this proposed method is effective and accurate at handling deflectometry measurement. © 2015 Optical Society of America

1. Introduction

In gradient measurement techniques, only normal fields or gradient data are acquired. To obtain a quality surface shape from these measurement data, an accurate 2D integration procedure is necessary. Currently, least-squares integration (LSI) method [1-4] and radial basis function integration (RBFI) method [5, 6] are widely used to reconstruct specular surface shape when gradient data is obtained by deflectometry, and many attempts at improvement have been researched. For example, G. Li [7] proposed a least-squares based integration method with high order truncation errors to reconstruct surfaces in the Southwell geometry, which is called high-order finite-difference-based least-squares integration method (HFLI) in the paper [3]. H. Ren [4] introduced an easy implementation integration method (EI-HFLI) based on HFLI to reconstruct gradient data locating at arbitrary domains. L. Huang [8] described an integration method by splitting a large size dataset into subsets, which are integrated by the RBFI method and then are stitched together with the least-squares method. Though these 2D integration methods can improve the reconstruction accuracy in some aspects, they still have some disadvantages. L. Huang gave a comparison of three of these 2D integration methods [3] , and pointed out that both the traditional LSI method and the cosine transform integration (CTI) method are easy and straightforward for dealing with large data sets but will introduce obvious shape errors if the gradient data does not have rectangular grids, and the RBFI method can handle gradient data in irregular grids but is mainly effective at handling small data sets. Practically, in a deflectometry measurement, the amount of gradient data is rather large, and data grids exist in quadrilateral or irregular shapes due to lens distortion and detection angle, as shown in Fig 1. This means that the traditional LSI method and RBFI method are not effective at directly handling this kind of measurement data. Though these measurement data can be interpolated into rectangular format [4] and then integrated via traditional LSI methods, this implementation is not so convenient.

With this in mind, we propose a new LSI method accounting for this disadvantage, which is based on an assumption that a regular surface at a given point can be approximated using Taylor's theorem by a polynomial. On the basis of this, within a tiny region around this point, the normal vector of this point can be seen as perpendicular to the vector connecting points at either side, as shown in Fig 2(a) and as described later. At the same time, a small measurement data sets integrated by the RBFI method is employed as a supplementary constraint of the new LSI method. In this paper, we call this method LSI-T, since this method is deduced from Taylor's Theorem. A detailed description is given in the next sections.

2. Principle of LSI-T method

2.1 Principle of deflectometry

Figure 1(a) exhibits a schematic illustration of deflectometry, where sinusoidal fringe patterns displayed on a LCD screen or ground glass are captured by a CCD camera after reflection by a specular surface.
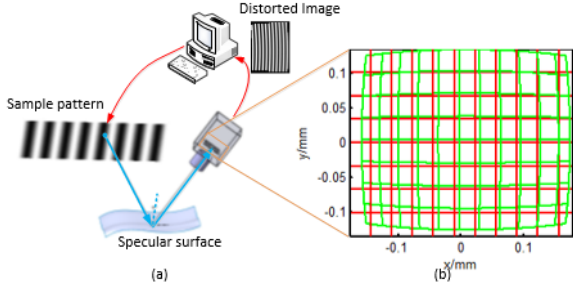
Fig. 1(a) Principle of deflectometry, (b) rectangular grids (red) becoming quadrilateral grids (green).

Fig. 2 Principle of LSI-T method in irregular grids

The captured patterns are deformed corresponding to the shape and curvature of the measured specular surface. Through analyzing the deformation, normal fields of this surface are obtained, which are then integrated to obtain the surface shape by related reconstruction algorithms. In a practical deflectometry system, lens distortion of a CCD imaging system and the specific perspective view of the CCD image used to observe the specimen will introduce additional dimensional changes of the sensor grids, which results in the normal vectors being located on the quadrilateral grids instead on the rectangular grids, as shown in Fig. 1(b). In this case, traditional LSI method cannot directly handle deflectometry measurement.

2.2 Height relation analysis from Taylor's theorem

We assume the measured regular surface can be expressed by an explicit function $z = f(x, y)$, and this function has at least two times differentiable at a given point. Then the surface at this given point can be approximated using Taylor's theorem [9] in two variables by a polynomial.

$$f(x + \Delta x_1, y + \Delta y_1) = f(x, y) + \frac{\partial f(x, y)}{\partial x}\Delta x_1 + \frac{\partial f(x, y)}{\partial y}\Delta y_1$$
$$+ \frac{1}{2}(\frac{\partial^2 f(x, y)}{\partial x^2}\Delta x_1^2 + 2\frac{\partial^2 f(x, y)}{\partial x \partial y}\Delta x_1 \Delta y_1 + \frac{\partial^2 f(x, y)}{\partial y^2}\Delta y_1^2) \quad (1)$$
$$+ R_2(\Delta x_1, \Delta y_1)$$

Where Δx_1 and Δy_1 are small real increments, approximation error $R_2(\Delta x_1, \Delta y_1)$ goes to zero faster than $\Delta x_1^2 + \Delta y_1^2$, i.e. faster than the smallest term in the approximation. Then Eq. (1) can be re-written in a more compact way using the vector $\nabla f(x, y)$ and the matrix of second derivatives $D^2 f(x, y)$ as

$$f(x + \Delta x_1, y + \Delta y_1) \approx f(x, y) + \nabla f(x, y) \cdot \binom{\Delta x_1}{\Delta y_1} + \frac{1}{2}\left(\binom{\Delta x_1}{\Delta y_1} \cdot D^2 f(x, y) \cdot \binom{\Delta x_1}{\Delta y_1}\right) \quad (2)$$

Where $\cdot$ denotes the scalar product. On the basis of the approximation function of Eq. (2), the relation between neighboring points and corresponding normal vectors can be deduced.

Assuming $(x_{m,n}, y_{m,n}, z_{m,n})$ are world coordinates of a given point of the measured surface, and the first and second differentiable of the surface at this point are $\nabla f(x, y)$ and $D^2 f(x, y)$. Within a tiny region around this given surface point, assuming two adjacent points $(x_{m,n+1}, y_{m,n+1}, z_{m,n+1})$ and $(x_{m,n-1}, y_{m,n-1}, z_{m,n-1})$ are each located at either side of point $(x_m, y_n, z_{m,n})$. According to Eq. (2), the relation between two neighboring points can be depicted as

$$\begin{cases} z_{m,n+1} - z_{m,n} \approx \nabla f(x, y) \cdot \binom{\Delta x_1}{\Delta y_1} + \frac{1}{2}\left(\binom{\Delta x_1}{\Delta y_1} \cdot D^2 f(x, y) \cdot \binom{\Delta x_1}{\Delta y_1}\right) \\ z_{m,n-1} - z_{m,n} \approx \nabla f(x, y) \cdot \binom{\Delta x_2}{\Delta y_2} + \frac{1}{2}\left(\binom{\Delta x_2}{\Delta y_2} \cdot D^2 f(x, y) \cdot \binom{\Delta x_2}{\Delta y_2}\right) \end{cases} \quad (3)$$

Where Δx_1 and Δx_2 are the increment of $x_{m,n}$ along $x_{m,n+1}$ and $x_{m,n-1}$, respectively. Similar with Δy_1 and Δy_2 along $y_{m,n+1}$ and $y_{m,n-1}$.
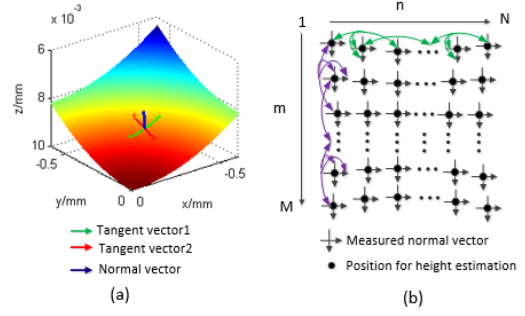
Subtracting the second equation of Eq. (3) from the first one, the relation between two separated points can be expressed as

$$z_{m,n+1} - z_{m,n-1} \approx \nabla f(x, y) \cdot \binom{\Delta x_1 - \Delta x_2}{\Delta y_1 - \Delta y_2}$$
$$+ \frac{1}{2}\left(\binom{\Delta x_1 - \Delta x_2}{\Delta y_1 - \Delta y_2} \cdot D^2 f(x, y) \cdot \binom{\Delta x_1 - \Delta x_2}{\Delta y_1 - \Delta y_2}\right) \quad (4)$$

Comparing Eq. (3) with Eq. (4), we can find that the second-order element of Eq. (4) is far smaller than the second-order element of Eq. (3). If the height relation is approximately expressed only by the first differentiable, Eq. (4) is more accurate than Eq. (3). In addition, the second-order element of Eq. (4) goes to zero faster than the first element. Thereby, Eq. (4) can be approximated as

$$z_{m,n+1} - z_{m,n-1} \approx f_x(\Delta x_1 - \Delta x_2) + f_y(\Delta y_1 - \Delta y_2)$$
$$= f_x(x_{m,n+1} - x_{m,n-1}) + f_y(y_{m,n+1} - y_{m,n-1}) \quad (5)$$

Where f_x and f_y are the first derivative of the surface. Similar relation between another two points $(x_{m+1,n}, y_{m+1,n}, z_{m+1,n})$ and $(x_{m-1,n}, y_{m-1,n}, z_{m-1,n})$ locating at either side of $(x_m, y_n, z_{m,n})$ can be deduced as

$$z_{m+1,n} - z_{m-1,n} \approx f_x(x_{m+1,n} - x_{m-1,n}) + f_y(y_{m+1,n} - y_{m-1,n}) \quad (6)$$

If a regular surface can be expressed by an explicit function, then the normal vector of one surface point can be depicted as $\langle f_x, f_y, -1\rangle$. Therefore, it can be concluded from Eq. (5) and (6) that normal vector of one point can be seen as perpendicular to the vector connecting points at either side, as shown in Fig. 2(a). Accordingly, the height relation between two separated points can be acquired as

$$\begin{cases} (z_{i,j+2} - z_{i,j}) = (x_{i,j+2} - x_{i,j}) \times f_{x(i,j+1)} + (y_{i,j+2} - y_{i,j}) \times f_{y(i,j+1)}, \\ \qquad i = 1 \cdots M, j = 1 \cdots N - 2; \\ (z_{i+2,j} - z_{i,j}) = (x_{i+2,j} - x_{i,j}) \times f_{x(i+1,j)} + (y_{i+2,j} - y_{i,j}) \times f_{y(i+1,j)}, \\ \qquad j = 1 \cdots M - 2, j = 1 \cdots N. \end{cases} \quad (7)$$

A visual description of Eq. (7) is shown in Fig. 2(b). Equation (7) can be written in terms of matrices as

$$\mathbf{D}_1 Z = G_1 \quad (8)$$

$$\mathbf{D}_1 = \begin{bmatrix} \mathbf{D}_1^x \\ \mathbf{D}_1^y \end{bmatrix} = \begin{bmatrix} \overset{2M+1}{\overbrace{\quad\quad}} \\ -1 & 0 & \cdots & 0 & 1 & \cdots & \cdots & \cdots & 0 \\ 0 & -1 & 0 & \cdots & 0 & 1 & \cdots & \cdots & 0 \\ \vdots & \vdots & \vdots & \vdots & \vdots & \vdots & \vdots & \vdots & \vdots \\ 0 & \cdots & \cdots & -1 & 0 & \cdots & \cdots & \cdots & 1 \\ \hdashline -1 & 0 & 1 & 0 & \cdots & \cdots & \cdots & \cdots & 0 \\ 0 & -1 & 0 & 1 & 0 & \cdots & \cdots & \cdots & 0 \\ \vdots & \vdots & \vdots & \vdots & \vdots & \vdots & \vdots & \vdots & 0 \\ 0 & \cdots & \cdots & \cdots & \cdots & \cdots & -1 & 0 & 1 \end{bmatrix}$$

$$[M \times (N - 2) + (M - 2) \times N] \times MN \quad (9)$$

Fig. 3 A small data set acting as supplementary constraints

$$G_1 = \begin{bmatrix} f_{x(1,2)}(x_{1,3} - x_{1,1}) + f_{y(1,2)}(y_{1,3} - y_{1,1}) \\ f_{x(2,2)}(x_{2,3} - x_{2,1}) + f_{y(2,2)}(y_{2,3} - y_{2,1}) \\ \vdots \\ f_{x(m,n+1)}(x_{m,n+2} - x_{m,n}) + f_{y(m,n+1)}(y_{m,n+2} - y_{m,n}) \\ \cdots\cdots\cdots\cdots\cdots\cdots\cdots\cdots\cdots\cdots\cdots\cdots\cdots\cdots \\ f_{x(2,1)}(x_{3,1} - x_{1,1}) + f_{y(2,1)}(y_{3,1} - y_{1,1}) \\ f_{x(3,1)}(x_{4,1} - x_{2,1}) + f_{y(3,1)}(y_{4,1} - y_{2,1}) \\ \vdots \\ f_{x(m+1,n)}(x_{m+2,n} - x_{m,n}) + f_{y(m+1,n)}(y_{m+2,n} - y_{m,n}) \end{bmatrix} \quad (10)$$

$$[M \times (N-2) + (M-2) \times N]$$

Equation (8) can be resolved by the Levenberg-Marquardt algorithm.

As seen from the aforementioned analysis, the expression in Eq. (7) does not require the measurement data to have South-well grids or rectangular formats. Thus, this integration method can deal with large measurement data with irregular grid shapes. However, Eq. (7) only gives a relationship between one point and every other data point. Therefore, a supplementary constraint between two neighboring points is needed to compensate the Eq. (8).

2.3 Supplementary constraint

Figure 2(b) shows the relation between one point and every other data point can be established via Eq. (7). If there are another two equations, one to establish the connection between two neighboring point along x axis and another one to build up a link between two neighboring points along y axis, then a relationship exists to link all the points together, as shown in Fig. 3(b). For constructing these kind of equations, the RBFI method is employed.

As shown in Fig. 3(a), a small data set less than 40 (pixel)×40 (pixel) ×2 (direction) but more than 4 (pixel)×4 (pixel) ×2 (direction) marked in brown is selected from the measurement, which is reconstructed by the RBFI method [5]. The principle of RBFI method and reconstruction process can be seen in [5]. Here we assume the selected data have a size of $M_1 \times N_1 \times 2$, and the reconstructed height data within this region is $z'_{m,n}$. Then the relationship between neighboring points within the selected region can be constructed as

$$\begin{cases} z_{i,j+1} - z_{i,j} = z'_{i,j+1} - z'_{i,j}, i = 1\cdots M_1, j = 1\cdots N_1 - 1 \\ z_{i+1,j} - z_{i,j} = z'_{i+1,j} - z'_{i,j}, j = 1\cdots M_1 - 1, j = 1\cdots N_1 \end{cases} \quad (6)$$

Where $z_{i,j}$ is the height in the world coordinate system and $z'_{i,j}$ is the reconstructed height data by the RBFI method. The above equation is rewritten in matrices as

$$\mathbf{D}_2 Z = G_2 \quad (12)$$

Where

$$\mathbf{D}_2 = \begin{bmatrix} \mathbf{D}_2{}^x \\ \mathbf{D}_2{}^y \end{bmatrix} = \begin{bmatrix} \overbrace{-1 \quad 0 \quad \cdots \quad 0}^{M_1+1} \quad 1 \quad \cdots \quad \cdots \quad \cdots \quad 0 \\ 0 \quad -1 \quad 0 \quad \cdots \quad 0 \quad 1 \quad \cdots \quad \cdots \quad 0 \\ \vdots \quad \vdots \quad \vdots \quad \vdots \quad \vdots \quad \vdots \quad \vdots \quad \vdots \quad \vdots \\ 0 \quad \cdots \quad \cdots \quad -1 \quad 0 \quad \cdots \quad \cdots \quad 1 \\ \cdots\cdots\cdots\cdots\cdots\cdots\cdots\cdots\cdots\cdots\cdots\cdots \\ -1 \quad 1 \quad 0 \quad \cdots \quad \cdots \quad \cdots \quad \cdots \quad 0 \\ 0 \quad -1 \quad 1 \quad 0 \quad 0 \quad \cdots \quad \cdots \quad 0 \\ \vdots \quad \vdots \quad \vdots \quad \vdots \quad \vdots \quad \vdots \quad \vdots \quad \vdots \quad 0 \\ 0 \quad \cdots \quad \cdots \quad \cdots \quad \cdots \quad \cdots \quad \cdots \quad -1 \quad 1 \end{bmatrix} \quad (13)$$

$$[M_1 \times (N_1 - 1) + (M_1 - 1) \times N_1] \times MN$$

$$G_2 = \begin{bmatrix} z'_{1,2} - z'_{1,1} \\ z'_{2,2} - z'_{2,1} \\ \vdots \\ z'_{m,n+1} - z'_{m,n} \\ \cdots\cdots\cdots\cdots \\ z'_{2,1} - z'_{1,1} \\ z'_{3,1} - z'_{2,1} \\ \vdots \\ z'_{m+1,n} z'_{m,n} \end{bmatrix} \quad (14)$$

$$[M1 \times (N1 - 1) + (M1 - 1) \times N1]$$

Combing Eq. (8) and Eq. (12), the new LSI method (LSI-T) is expressed as

$$\begin{bmatrix} \mathbf{D}_1 \\ \cdots \\ \mathbf{D}_2 \end{bmatrix} Z = \begin{bmatrix} G_1 \\ \cdots \\ G_2 \end{bmatrix} \quad (15)$$

Thus, when the normal data of the detected surface and corresponding x and y position are known or have been calculated by other methods, the height data can be calculated via Eq. (15) by the Levenberg-Marquardt algorithm whether the data is located on a regular or irregular rectangular grids.

3. Simulation

To investigate the feasibility of the LSI-T method and to verify its accuracy in comparison to the traditional LSI method, numerical simulations for data located at rectangular grids and quadrilateral grids are performed via LSI-T, HFLI and EI-HFLI methods. The HFLI method represents one typical LSI method to reconstruct the measurement data having rectangular grids. When the data has irregular grids shape, the EI-HFLI method will interpolate the measurement data first to format them into rectangular grids data, and then reconstruct them.

3.1 Simulation on rectangular grids

A concave spherical surface is simulated as shown in Eq. (16). The circular measurement range of this surface is -25 mm to 25 mm for both x and y direction, and the points' interval is 50 μm, as shown in Fig. 4.
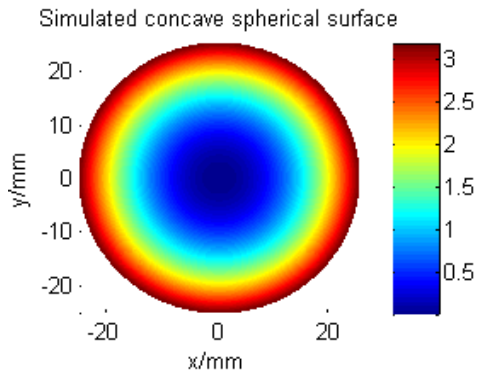
$$z = -\sqrt{10000 - x^2 - y^2} \quad (16)$$

Fig. 4 Simulated concave spherical surface
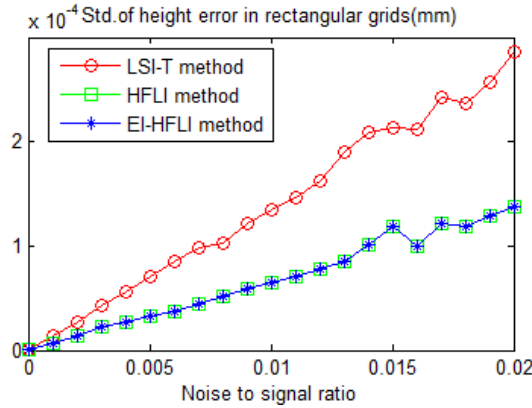
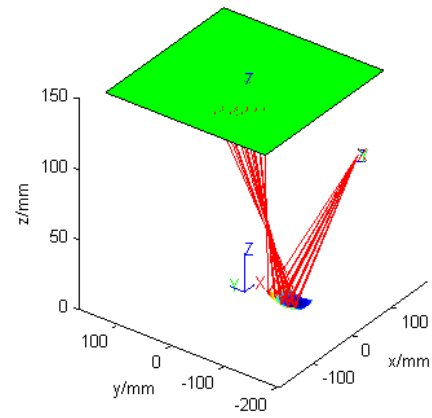Fig. 5 RMS value of reconstruction errors when data are in rectangular grids

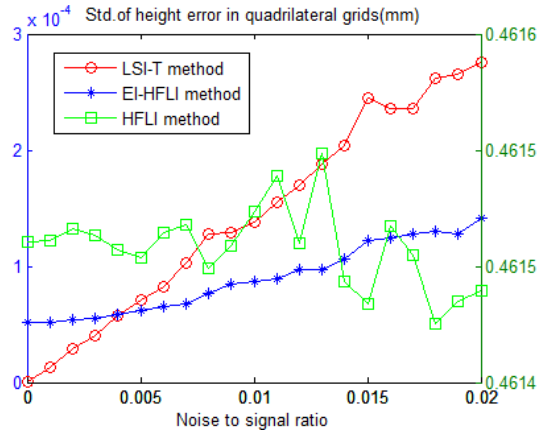Fig. 6 Concave surface is simulated in a deflectometry system

Fig. 7 RMS value of reconstruction errors when data are in quadrilateral grids (red and blue data corresponds to y axis on the left, green data corresponds to right label)

The normal vector of this surface at each point can be calculated by differentiating the simulated function. To investigate the performance of these integration methods under noise condition, random noises with noise to signal ratio from 0% to 2% are added to the gradient data. When the data is distributed uniformly on the rectangular grids, Fig. 5 shows how the standard deviation (Std.) of the errors changes based on different noises. As depicted in Fig. 5, all the three methods can achieve better than sub-micrometer results, though the LSI-T method exhibits an inferior result compared to the EI-HFLI and HFLI, which may be result from the exclusion of the second-order element of Eq. (4). The effect of the high-order element of Taylor's expansion on the reconstruction accuracy using the LSI-T method will be analyzed in another paper.

3.2 Simulation on quadrilateral grids

For verifying the performances of the integration method under non-rectangular grid conditions, a similar simulation is carried out. Here the concave surface described using Eq. (16) is assumed to be measured by deflectometry, as shown in Fig. (6). The CCD camera with lens-distortion parameters [-0.1196 0.3236 0 0] observes the detected surface with a given perspective. Due to the lens distortion and perspective view of the CCD camera, the captured data is not on a rectangular grid.

Similarly, random noise with noise to signal ratio from 0% to 2% are added to the gradient data. The RMS value of standard deviation of the errors is shown in Fig. 7, where the HFLI method gives the poorest reconstruction quality with RMS value around 0.4615 mm, while the LSI-T and EI-HFLI methods more give satisfactory results. When the noise to signal ratio is more than 0.5%, the EI-HFLI method has a better reconstruction accuracy than LSI-T, which also may be the influence of the exclusion of the high-order element of Eq. (4). When the noise is less than 0.5%, the LSI-T method gives the best results. In the EI-HFLI method, an interpolation process is used to transfer the irregular grid data into rectangular grid format. In addition, comparing the reconstruction error of Fig. 5 and Fig. 7, it can be concluded that grids

format has nearly no influence on the reconstruction result of EI-HFLI method because of the interpolation operation but has a strong affect for the HFLI method. For the LSI-T method, it is also seldom affected by grid format and can achieve a high-accuracy reconstruction.

4. Experiments

Measurements have been conducted to investigate the feasibility and verify the reconstruction accuracy of the LSI-T method in a stereo-deflectometry system. A 2 inch optical flat surface with flatness $\leq \lambda / 10$ and a 2 inch concave surface with $76.2^{+0.0}_{-0.2}$ mm radius are measured.

When the flat surface is inspected by stereo deflectometry, Fig. 8 shows the calculated normal vectors distribution and corresponding errors along x direction for the 86% range of the whole surface. The root mean squares (RMS) value of the gradients along x is approximately 3.75×10^{-5} radian. The gradients along the y direction and the associated error distribution are shown in Fig. 9, and RMS value of the errors is 9.26×10^{-5} radian. In order to make a comparison between the proposed method and the LSI method, the calculated gradients are reconstructed by the EI-HFLI and LSI-T method, respectively. Before the gradients of Fig. 8 and Fig. 9 are integrated by the EI-HFLI method, the data are transformed into rectangular grids with spacing of 56.1 μm along the x axis and 56.2 μm along the y axis by interpolation. Then the formatted gradients are reconstructed by the EI-HFLI method as shown in Fig. 10(a). Fig. 10(b) shows the error distribution, with an RMS value of approximately 155.05 nm. When applying the LSI-T method, a small data set with 5 (pixel) ×5 (pixel) ×2 (direction) is selected to be reconstructed by RBFI method as the
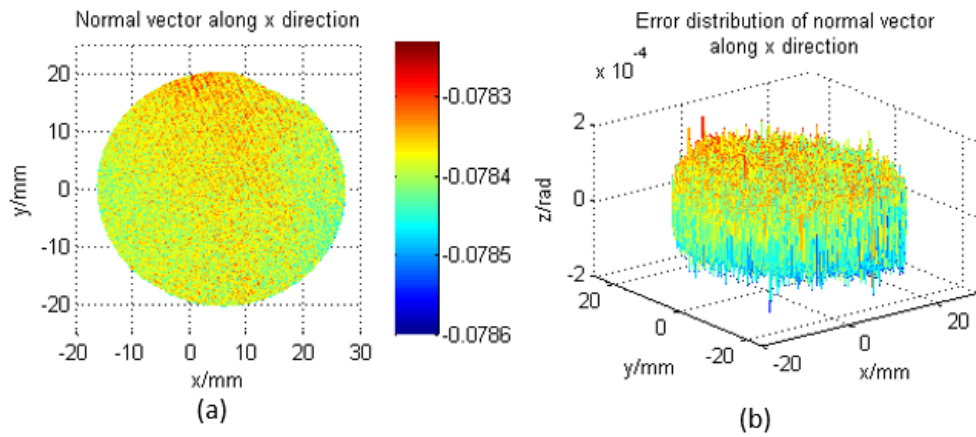
Fig. 8 Normal vector distribution along x direction (a) and its errors (b)
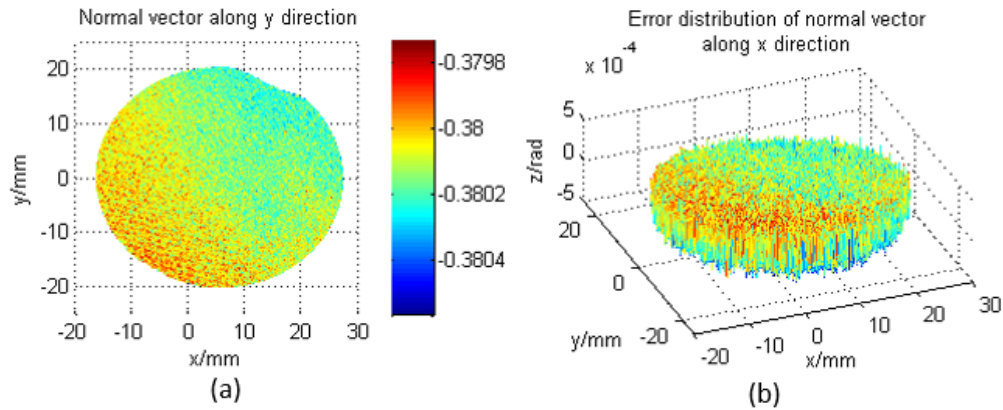

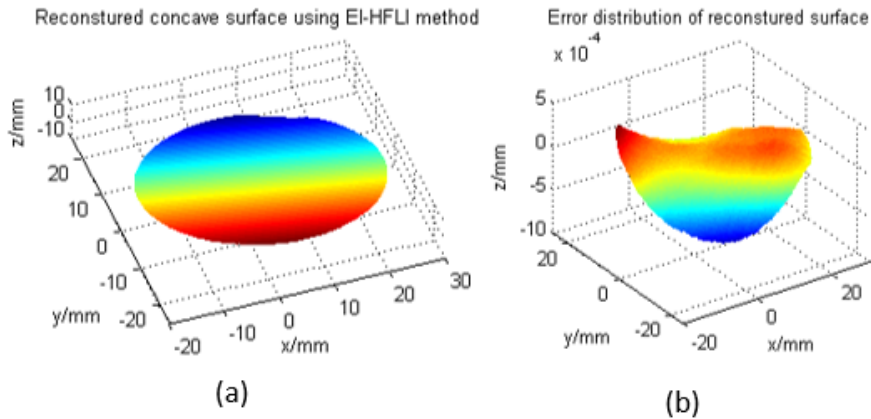Fig. 9 Normal vector distribution along y direction (a) and its errors (b)

Fig. 10 Reconstructed surface using RBFI method within selected region
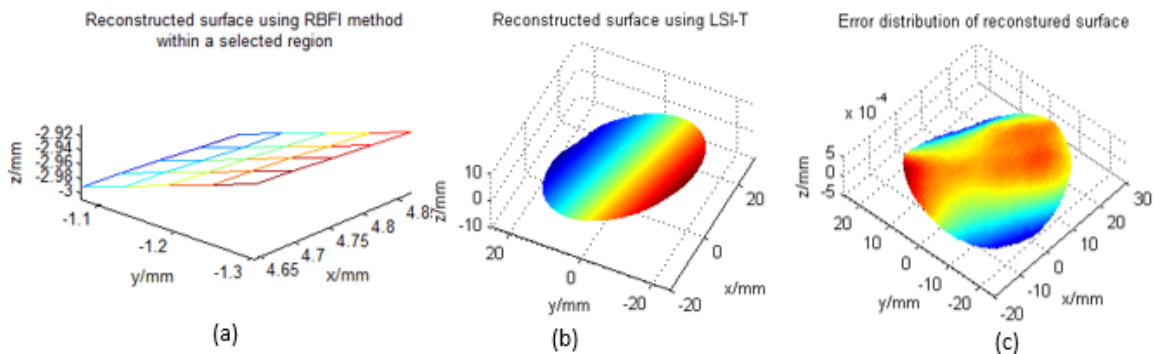

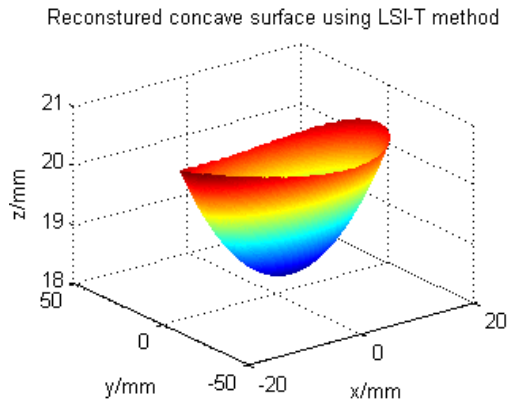Fig. 11 Reconstructed surface by LSI-T (a) and its error distribution (b)

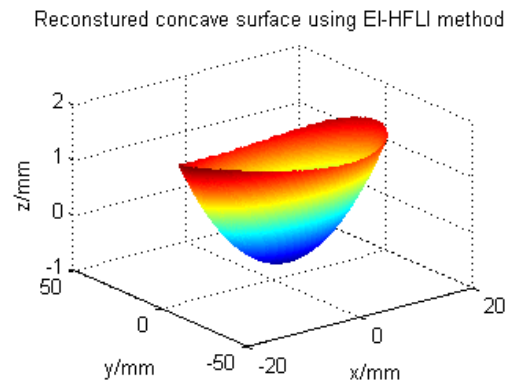Fig. 12 Reconstructed concave surface with LSI-T
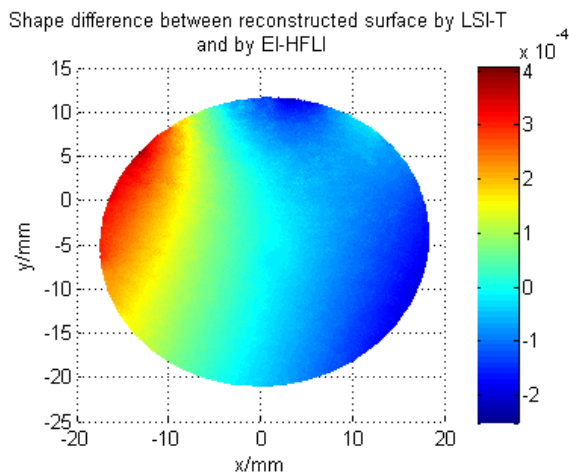

Fig. 13 Reconstructed concave surface using EI-HFLI

Fig 14 Shape difference between reconstructed surface by LSI-T and EI-HFLI

supplementary constraints, as shown in Fig. 11(a). On the basis of the calculated gradients data and the constraints data, the reconstructed surface using the LSI-T method is shown in Fig. 11(b), and its error distribution is as Fig. 11(c). The RMS value of which is approximately 152.9 nm. As seen from the error distribution in Fig. 11(c) and Fig. 10(b), it can be deduced that the LSI-T method can be used to reconstruct the gradients directly and have a comparable reconstruction results with the EI-HFLI method.

The same procedure is applied to measure the 2 inch concave surface. Fig. 12 shows the reconstructed surface using the LSI-T method, and Fig. 13 depicts the integrated surface shape using the EI-HFLI method. The shape difference between the two reconstructed surfaces is shown in Fig. 14, the RMS value of which is 119.97 nm. The data in Fig. 14 demonstrates the proposed method is feasible and accurate. In addition, if the reconstructed surface is fitted using a spherical function, the radius of the surface in Fig. 12 is 76.3153 mm, and the surface radius in Fig. 13 is 76.3162 mm. This small difference in radius of 0.9 μm illustrates the comparability of the proposed method to that of the EI-HFLI method.

5. Conclusions

For some gradient measurement methods, the captured gradient data are not uniformly distributed on a rectangular grid because of lens distortion or other reasons. In this case, the traditional LSI method or RBFI method are not direct or convenient to reconstruct the gradients. This paper proposes a new LSI method based on the approximation that the normal vector of a point is perpendicular to the vector connecting points at either side. Simulation shows that the grid format rarely has an effect on the reconstruction accuracy for the LSI-T method, but has a strong influence on the LSI methods. Though the EI-HFLI method can be used to integrate the gradients data by formatting them into rectangular grids, this method is not so direct and convenient. Experiments demonstrate that LSI-T is effective at handling data from gradient measurement techniques when data grids are not uniform and is comparable with the EI-HFLI method.

Reference

1. W. H. Southwell, "*Wave-front estimation from wave-front slope measurements,*" J. Opt. Soc. Am. **70,** 998-1006 (1980).
2. L. Huang, and A. K. Asundi, "*Improvement of least-squares integration method with iterative compensations in fringe reflectometry,*" Appl. Opt. **51,** 7459-7465 (2012).
3. L. Huang, M. Idir, C. Zuo, K. Maznatcheev, L. Zhou, "Comparison of two-dimensional integration methods for shape reconstruction from gradient data," Opt. Lasers Eng. **64,** 1-11 (2015).
4. H. Ren, F. Gao, and X. Jiang, "*Improvement of high-order least-squares integration method for stereo deflectometry,*" Appl. Opt. **54,** 10249-10255 (2015).
5. S. Ettl, J. Kanimski, M. Knauer, and G. Häusler, "Shape reconstruction from gradient data," Appl. Opt. **47**, 2091-2097 (2008).
6. S. Lowitzsch, J. Kaminski, M. C. Knauer, and G. Häusler, "Vision and modeling of specular surfaces," in *Vision, Modeling, and Visualization 2005*, G. Greiner, J. Hornegger, H. Nicemann, and M. Stamminger, eds. (Akademische Verlagsgesellschaft Aka GmbH, 2005), pp. 479-486.
7. G. Li, Y. Li, K. Liu, X. Ma, and H. Wang, "Improving wavefront reconstruction accuracy by using integration equations with higher-order truncation errors in the Southwell geometry," J. Opt. Soc. Am. A **30**, 1448-1459 (2013).
8. L. Huang, and A.K. Asundi, "Framework for gradient integration by combining radial basis functions method and least-squares method," Appl. Opt. **52**, 6016-6021 (2013).
9. V. A. Zorich, *Mathematical Analysis I (*Springer, 2002).